High-Fidelity Simulations of Lift+Cruise VTOL Urban Air Mobility Concept Aircraft in Hover

Yi Liu* and Li Wang†
NASA Langley Research Center, Hampton, Virginia 23681, USA

This paper presents progress of high-fidelity multidisciplinary simulations for the NASA lift+cruise vertical takeoff and landing (VTOL) urban air mobility concept aircraft in hover. The study focuses on the unsteady flow solutions featuring strong wake interactions between rotors and the airframe. The simulations couple a high-fidelity aerodynamic model with a comprehensive rotorcraft aeromechanics tool with rotor rotation-speed trim. The aerodynamic model is based on the Reynolds-averaged Navier-Stokes equations using the one-equation Spalart-Allmaras turbulence model with rotation correction. Unsteady aerodynamic flows are computed on a dynamic, deformable, unstructured, overset grid system. An integrated overset-grid assembler is used to construct the composite grid from 23 component grids and facilitate communications between individual component grids. Rotor performance and airframe forces and moments are computed and compared on two unstructured grids. The study demonstrates capabilities of high-fidelity multidisciplinary analysis tools to capture the strong unsteady flowfield around this multi-rotor aircraft in hover.

I. Introduction

Rotorcraft performance in hover is an important design consideration as it represents a limiting condition in terms of power requirements. To assess and advance the state-of-the-art computational method to accurately predict hover performance, an AIAA sponsored Rotorcraft Hover Prediction Workshop (HPW) was initiated in 2014 [1]. The vision of HPW is "to inspire collaboration among industry, governments, and academia for the development of computational methods to predict all aspects of hovering flight efficiently, practically, and accurately." Over the past nine years, computational studies by researchers around the world have been presented at the annual HPW meetings at AIAA SciTech forums. The summary of the HPW papers and other activities are available at the website cited in Ref. [2].

Previous HPW studies largely focused on a single isolated rotor in hover and validation against test data. Three sets of test data (the Sikorsky S-76 rotor [3], the Pressure Sensitive Paint rotor [4] and the Hover Validation and Acoustic Baseline blades [5]) are available. Significant improvements in hover predictions for these three rotors have been reported [6–16] using adaptive mesh refinement, advanced turbulence/transition modeling, and accounting for aeroelastic effects. However, only a few studies have addressed the rotor/airframe interactions in hover [17–18] or conducted simulations for unmanned aerial vehicles (UAVs) [19] in hover. For HPW at SciTech 2024, a call for more general calculations for eVTOL or UAV aircraft in hover was announced [2]. This paper presents simulation results for a multi-rotor VTOL aircraft in hover contributing to ongoing research efforts in this direction.

Currently the NASA Revolutionary Vertical Lift Technology (RVLT) project is conducting research in urban air mobility (UAM) aircraft and operations, which is a subset of advanced air mobility. UAM focuses on highly automated aircraft that operate and transport passengers or cargo at low altitudes within urban and suburban areas featuring vertical takeoff and landing, and efficient cruise flight capabilities. The NASA RVLT project is developing UAM VTOL concept vehicles [20–23] to guide aircraft development for emerging aviation markets. NASA concept vehicles provide specific configurations for the NASA UAM

* Research Aerospace Engineer, Computational Aerosciences Branch, Senior Member AIAA
† Research Aerospace Engineer, Computational Aerosciences Branch, Associate Fellow AIAA

research. The lift+cruise VTOL aircraft is one of the three UAM conceptual configurations recently presented [21].

The RVLT project also supports development of cutting-edge technology and tools for analyzing and designing VTOL vehicles that can operate safely and reliably with reduced environmental impact. Current multidisciplinary analysis tools and workflows, from a lower-fidelity comprehensive analysis tool to higher-fidelity multidisciplinary simulations, have been applied to a variety of VTOL concept vehicles. Johnson and Silva [24] performed comprehensive analysis of several VTOL UAM concepts. Subsequently, Diaz et al. performed high-fidelity computational fluid dynamics (CFD) simulations of NASA's side-by-side air taxi concept [25], NASA's quiet single-main rotor helicopter concept [26], NASA's quadrotor concept [27], and NASA's tilt-wing concept [28] using a CFD solver, OVERFLOW [29], loosely coupled with the Comprehensive Analytical Model of Rotorcraft Aerodynamics and Dynamics II (CAMRADII) model [30]. Recently, Caprace et al. studied the full and partial ground effects from a single rotor and a quadrotor in hover [31]. Druyor and Wang [32] conducted a high-fidelity analysis of a six-passenger quadrotor air taxi concept vehicle using a finite-volume, unstructured-grid, CFD solver, FUN3D [33], coupled with CAMRADII. Our previous study [34] used the FUN3D/CAMRADII coupling workflow to predict the lift+cruise aircraft rotor performance in hover and low-speed forward flight conditions with collective pitch trim. It demonstrated that including a rotation correction to the Reynolds-averaged Navier-Stokes (RANS) formulation based on the SA-neg [35] turbulence model significantly improves the resolution of secondary vortices and wake interactions at the same grid-resolution level, especially for hover simulations. This enhanced turbulence model, designated as SA-neg-R at the turbulence modeling resource (TMR) website[‡], is based on the work of Dacles-Mariani [36] to reduce the turbulent eddy viscosity levels in the vortex-core region. In the previous study, significant unsteadiness in the force distributions on the rotor disk planes was observed in hover, but the history data of the airframe forces were not presented in the analysis.

In this paper, we investigate the hover performance of the lift+cruise multi-rotor aircraft, where strong rotor/rotor and rotor/airframe interactions through the rotor wake are expected. Coupled FUN3D/CAMRADII simulations of this aircraft are conducted for the hover condition on two unstructured, overset grids, a baseline grid with 208 million grid points, which is the same grid used in the previous study [34], and a new, finer grid containing 394 million grid points, offering refined mesh resolution in the nearfield and wake regions.

The material in the rest of this paper is presented in the following order. Section II briefly describes the multidiscipline models and the loose-coupling process. Section III describes the lift+cruise VTOL UAM concept aircraft and the finer CFD composite grid system. Section IV presents the multidisciplinary analysis of the aircraft in a hover condition and compares solutions computed on the baseline grid and the finer grid. Section VI contains concluding remarks and plans for future work.

II. Multidisciplinary Analysis

This section overviews the models used in the multidisciplinary analysis of the lift+cruise VTOL aircraft. A brief description of the loose-coupling process is also provided.

A. CFD solver

CFD solutions are computed by FUN3D [33], developed and maintained by NASA Langley Research Center. FUN3D is a node-centered, unstructured-grid flow solver, which is widely used for high-fidelity analysis and adjoint-based design of complex turbulent flows [38–42]. In this study, FUN3D solves RANS equations discretized on unstructured mixed-element grids that contain tetrahedra, pyramids, prisms, and hexahedra. The residuals are evaluated on a set of median-dual control volumes centered at grid points. Edge-based inviscid fluxes are computed at edge midpoints using an approximate Riemann solver. In the current study, Roe's flux-difference splitting [43] is employed. For second-order accuracy, density,

[‡]https://turbmodels.larc.nasa.gov/spalart.html; Accessed October 2023

pressure, and velocities are reconstructed to edge midpoints by a UMUSCL (unstructured monotonic upstream-centered scheme for conservation laws) scheme [44–45]. For the discretization of viscous fluxes, the Green-Gauss theorem is used to compute cell-based gradients. For nontetrahedral grids, cell-based Green-Gauss gradients are combined with edge-based gradients [46–47] to improve the stability of viscous operators and prevent odd-even decoupling. The SA-neg-R turbulence model is used in the current study. To advance in time, a library of implicit time integration schemes is available. In the current work, a second-order backward difference scheme, BDF2opt [48], is used.

Recently, a new overset-grid assembler for unstructured-grid systems, Yoga [49], has been developed and integrated into FUN3D. Yoga is a parallel overset-domain assembly code that uses a modified wall-distance criterion to select overset boundary locations and leverages dynamic load balancing to achieve high performance on thousands of MPI processing cores. Yoga improves computational scalability of overset-grid assembly for rotorcraft simulations allowing for computations on larger grid systems. As demonstrated by previous studies [32], Yoga's new overset capability is critical for CFD simulations of complex VTOL aircraft involving multiple rotors with many blade components (e.g., 22 moving bodies for this lift+cruise aircraft). A relatively large composite overset-grid system is required to capture detailed wake effects from multiple rotor blades.

B. Comprehensive analysis modeling

A comprehensive analysis model, CAMRADII has been developed by Johnson [30] and used for structural dynamics calculations of the rotor blades and trim solutions of the aircraft. CAMRADII incorporates various advanced computational models including multibody dynamics, nonlinear finite elements, structural dynamics, and rotorcraft aeromechanics. Each blade is modeled as a set of nonlinear beam elements. This structural-dynamics analysis accurately assesses blade deflections and structural responses to aerodynamic loads. The internal aerodynamics model in CAMRADII is a low-fidelity approximation based on the lifting-line theory and vortex-wake models. In addition, CAMRADII provides rotor trim solutions for a specific flight condition using either collective pitch trim or variable rotation-speed trim, which is also called RPM (revolution per minute) trim. Our previous study [34] focused on the use of rotor collective pitch trim control. In the current study, the rotor RPM trim is utilized since it is more frequently used for small multi-rotor UAV aircraft because the control mechanism is relatively simple and lightweight. The CAMRADII model of lift+cruise aircraft was built during the concept design stage [21, 50]. It is a necessary step in multidisplinary high-fidelity simulations, as the blade motion, rotor trim and vehicle trim are usually obtained by a comprehensive analysis coupled with CFD airloads.

C. Loose coupling process

The first FUN3D/CAMRADII interface to exchange aerodynamic loads and structural responses was developed and reported in 2008 [51]. In recent years, this interface has been updated and extended to enable multidisciplinary analysis of multiple rotors with various blade radii, and different rotational directions and speeds. In the current study, this interface is further extended to compute and report unsteady forces and moments on the airframe components, such as fuselage, wings, tail fins, and tail wings, etc., separately.

Figure 1 shows the file-based loose-coupling workflow [32] used in the current simulations. In a loose-coupling procedure, the interactions between a high-fidelity CFD solver and a comprehensive-analysis solver occur at the end of each coupling cycle. The exchange of CFD airloads and structural deflections is performed through file I/O. Translator code is employed to manage data in the formats required by CAMRADII and FUN3D.

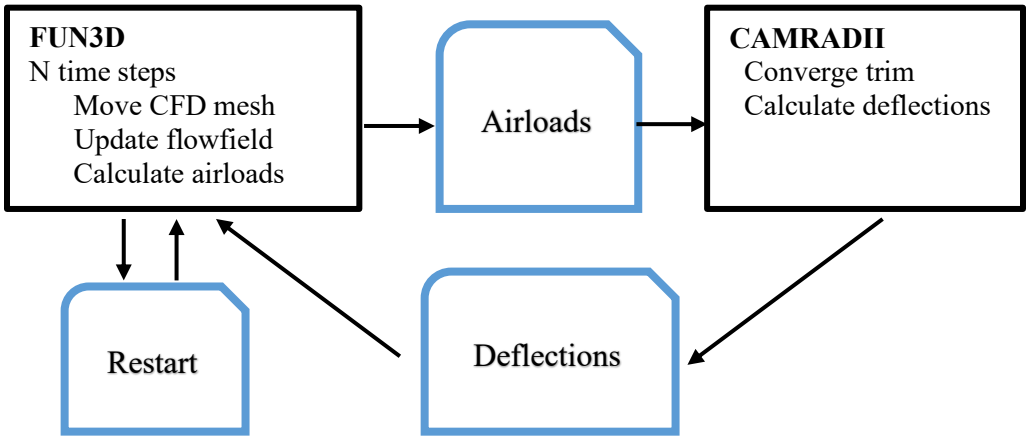

Figure 1. File-based loose-coupling workflow.

III. Lift+Cruise VTOL Aircraft and CFD Grids

This section briefly describes the lift+cruise VTOL concept aircraft and the CFD grids used for hover simulations.

A. Lift+Cruise VTOL aircraft

The lift+cruise VTOL concept aircraft [21] is a compound helicopter configuration featuring lifting rotors and wings for thrust and lift, and a rearward-facing propeller for enhanced aerodynamic efficiency in forward flight. The vehicle is designed to operate as a fixed-wing aircraft during cruise flight, when the lifting rotors do not rotate, and forward thrust is provided by a pusher propeller. The lift rotors operate during the VTOL takeoff and landing phases of flight. In the hovering phase, only the lift rotors are in motion, while the back pusher remains stationary. This configuration is commonly referred to as the helicopter mode.

Figure 2 shows a computer-aided-design (CAD) model of the lift+cruise aircraft based on the concept configuration from Ref. [21]. It has eight lifting rotors mounted on the wing and a single pusher propeller. The rotor numbering follows a convention that is common for multiengine fixed wings, left-to-right, front-to-back. In Fig. 2, the number and the rotation direction are indicated for each rotor. The propeller is also referred to as rotor 9. Each lifting rotor has two blades, which are aligned with the travel direction during cruise flight to minimize the drag penalty. The propeller has six blades to produce adequate forward thrust. In the current design, the radius of the lifting rotor blades is 5 feet with a linear taper of 0.75 and a linear twist of -15 degree from the hub center to the blade tip. The rotor blade mean chord is 1.2277 feet. The radius of the propeller blade is 4.5 feet with a linear taper of 0.75 and a linear twist of -35 degree. Both blades use the VR12 airfoil from r/R = 0 to 0.85 and the SSC-A09 airfoil between r/R = 0.95 and the tip, with a linear blend between them from r/R = 0.85 to 0.95.

Figure 3 shows the surface model of the lift+cruise aircraft fuselage imported to the Pointwise[§] software, from top and side view directions. The x, y, and z axes indicate the origin of the model, which is consistent with the CAMRADII model specification. Table 1 lists the weight and dimensions of the lift+cruise aircraft and the centers of several airframe components. Detailed geometry information about the lifting rotors can be found in Ref. [34] and are not listed here.

[§] https://www.pointwise.com; Accessed November 2023

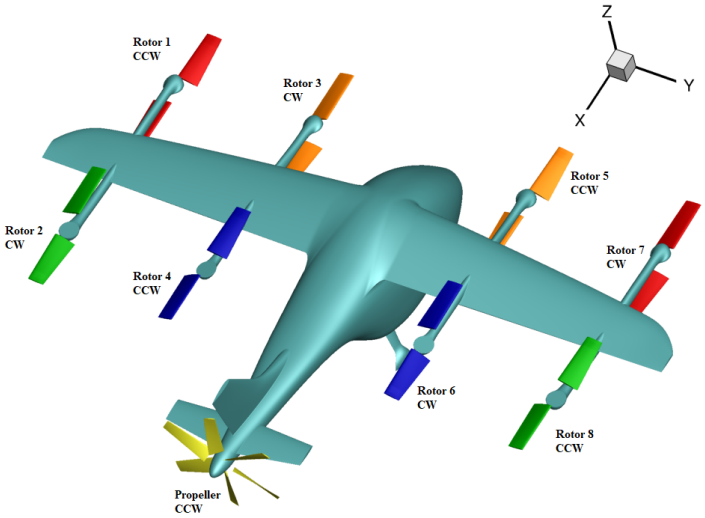

Figure 2. CAD surface model of lift+cruise aircraft.
(CCW – counter-clockwise rotation; CW – clockwise rotation)

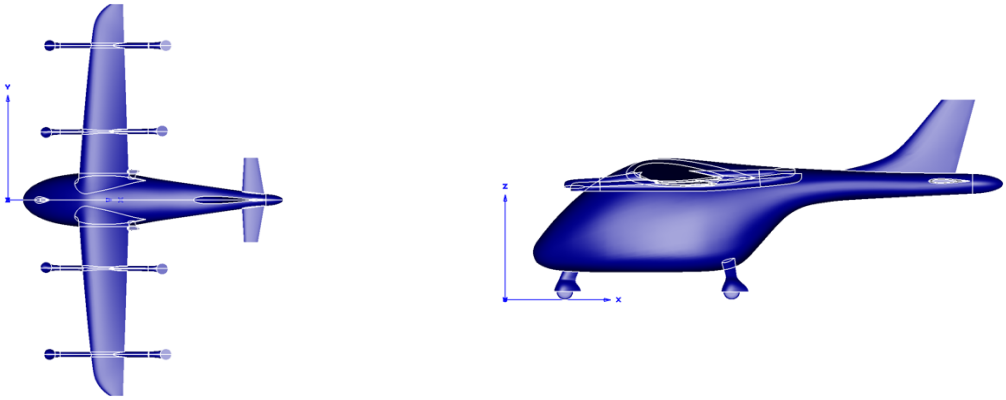

Figure 3. Pointwise surface model of lift+cruise aircraft fuselage.

Table 1. Lift+Cruise concept aircraft geometry parameters.

Vehicle	Dimensions
Weight	5903 *lb*
Length	31.58 *ft*
Height	13.47 *ft*
Main Wing Full Span	47.69 *ft*
Tail Wing Full Span	10.32 *ft*
Radius of Lift Rotor	5.00 *ft*
Radius of Propeller	4.50 *ft*
Center of Gravity	12.0, 0.0, 0.0 *ft*
Center of Wing-body	10.69, 0.0, 8.5 *ft*
Center of Propeller Hub	31.94, 0.0, 7.79 *ft*
Center of Horizonal Tail	29.1, 0.0, 8.01 *ft*

B. CFD composite grid systems

Composite, overset, unstructured-grid systems have been generated for high-fidelity CFD analysis performed by FUN3D. There are four types of component grids: near-body grids for clockwise (CW) and counterclockwise (CCW) rotating lifting-rotor blades, near-body grids for propeller blades, and a background grid that includes fuselage, wings, tails, and other stationary components. The composite grid has a total of 23 components including 16 lifting rotor blade grids, six propeller blade grids and the fuselage background grid, assembled using Yoga. Two grids have been used for grid convergence studies. The baseline grid with 208 million grid points is the grid used in Ref. [34]. A finer grid has been created containing around 394 million grid points to offer enhanced mesh resolution in the nearfield and wake regions. The grid systems are expressed in terms of feet, consistent with the physical characteristic length of the aircraft.

Details about the baseline grid can be found in Ref. [34] and will not be repeated here. For the finer grid, the component grid for the lifting rotor blades contains around 4.2 million grid points. At the rotor surface, grid points are added along the chordwise direction. The grid shortest distance to the wall is still at 0.00001 grid unit, which corresponds to a y^+ around 1. Many grid points are added into the isotropic tetrahedral region of the volume grid controlled by a cylinder-shape source in Pointwise software, as shown in Fig. 4. The maximum edge length of this grid is around 7.5% of the blade mean chord length. The longest edge is located at the blade root cut region where anisotropic tetrahedra are generated in transition from the boundary layer prisms to the isotropic tetrahedra. In other regions, most edge lengths are less than 5% of the chord length.

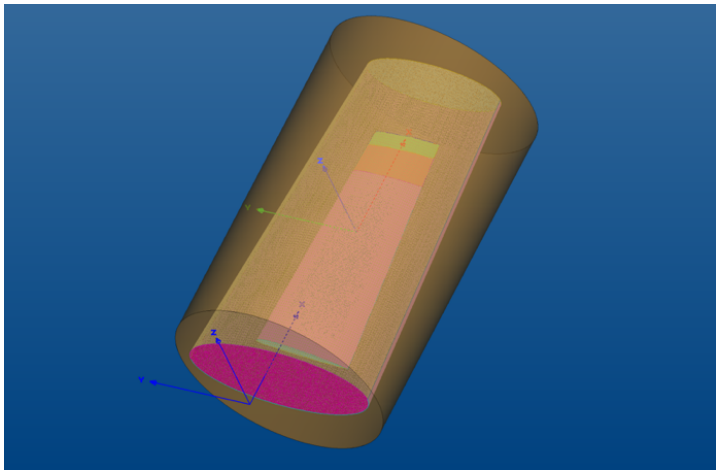

Figure 4. The rotor blade grid with a cylinder-shape source region (CCW rotation).

For the fuselage background grid shown in Fig. 5, four cylinder-shape source regions for the lifting rotors have been significantly enlarged to better capture rotor wakes. Compared to the baseline grid, the radius of cylinder is increased from 1.2 to 2 rotor radii. The length of the cylinder is increased from 2.4 to 4 rotor radii. The spacing control parameter of the cylinder source is set to 0.05 grid unit, which is less than 5% of the chord. The background grid has prism layers near the fuselage surface and transitions to tetrahedral in the off-body region. Since the grid is generated for hover simulations, when the propeller is stationary, the propeller blade component grid is kept the same as in Ref. [34], and the cylinder source region around the propeller is removed.

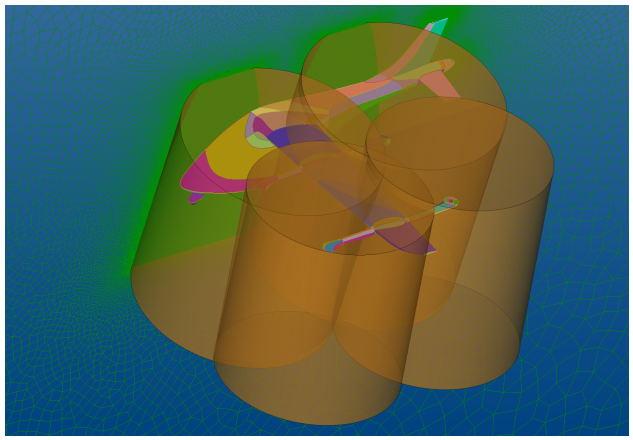

Figure 5. The fuselage background grid with cylinder-shape source regions. (Half symmetry domain)

Overall, the full fuselage background grid contains approximately 320 million points. The new composite grids, which includes the fuselage, rotors, wings, and propeller has 394 million points. As shown in Fig. 6, the region with clustered points encompasses a significant portion of the fuselage and extends much further beyond the fuselage, rotor blades, and landing gears. Compared to the baseline grid, this finer grid allows for better capturing of the rotor wake characteristics and more details of the wake/airframe interactions.

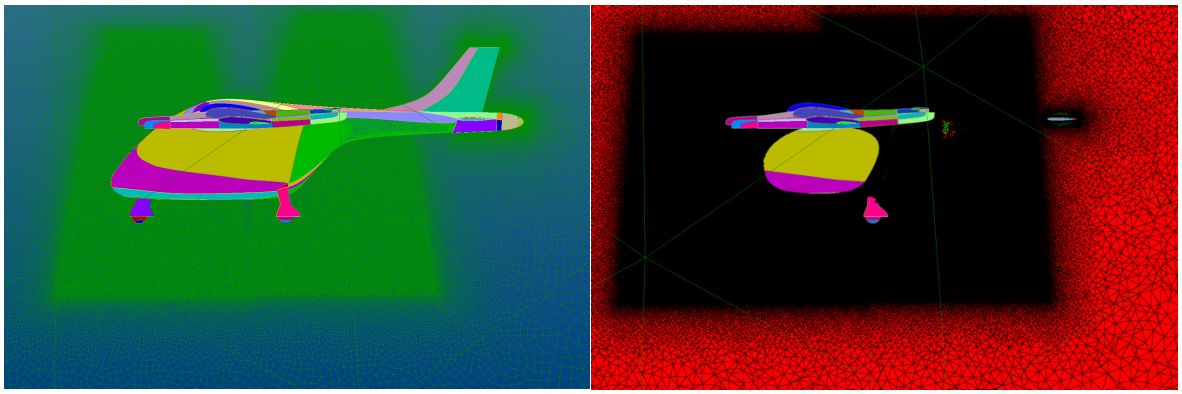

a. Grid cut at y = 0, symmetry plane

b. Grid cut at y = 3

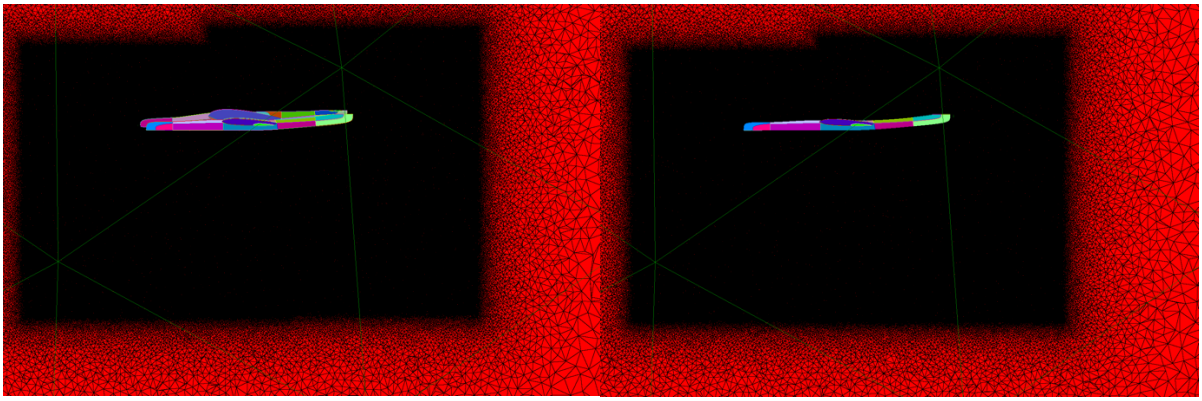

c. Grid cut at y = 8.13
(Front inboard rotor rotation center)

d. Grid cut at y = 18.75
(Outboard rotor rotation center)

Figure 6. Grid cuts at different y locations illustrating background grid resolution.

IV. Hover Results

In this section, high-fidelity multidisciplinary analyses of the lift+cruise aircraft for the hover condition are presented and solutions on the baseline and finer grids are compared.

A. Hover Conditions and Coupling Cycles

In hover, the lifting rotors are operational, whereas the pusher propeller is stationary. The starting rotational speed of each lifting rotor is 1050.42 RPM with a nominal tip speed of 550 ft/sec. The standard atmosphere condition at 5000 *ft* altitude and a temperature of 77.17 ^{o}F are applied in CAMRADII and adopted for FUN3D simulations, which correspond to a tip Mach number of 0.4842, a tip Reynolds number of 2.74 million per foot (grid unit), and temperature of 298.24 K. With variable RPM trim, the rotation speed is adjusted between coupling cycle until the coupled system reaches a convergence state. In CAMRADII, the trim targets are the vehicle net z-force (lift-weight) and x-force (drag direction), and the combined rotor y-moment (pitching moment); these forces and moment are trimmed to be zero by varying the rotation speeds of the lifting rotors. In the current CAMRADII RPM trim control setting, the four front rotors are linked together to maintain the same rotation speeds and the four back-rotors' rotation speeds are the same as well. The collective pitch angles for all rotor blades are fixed at 12.15 degrees. Besides the rotation speeds of the lifting rotors, CAMRADII sets the aircraft pitch angle as an additional trim parameter. In the present CAMRADII setting, the fuselage-wing aerodynamic forces and moments are set as zero for the hover condition. As discussed in section IV.C, in future work, these forces and moments will need to be updated based on high-fidelity CFD predictions.

The CFD is initialized with freestream conditions and implicitly advanced in time with a time step corresponding to 0.5 azimuth degree of the slowest rotor to accommodate different rotor rotation speeds in RPM trim, such that all rotors have a full revolution of airloads data at the end of each coupling cycle to be used by CAMRADII. Eight subiterations are conducted at each time step during which the combined meanflow and turbulence-model residuals are reduced by about four orders of magnitude. The first coupling cycle (for which CFD simulations start with a uniform-flow initial condition) is advanced a full revolution (360 degrees, 720 time steps); in all other coupling cycles, the CFD simulation period corresponds to a half revolution (180 degrees, 360 time steps). A total of 31 coupling cycles were performed using both grids, which correspond to 16 revolutions for the slowest rotor.

Figure 7 shows the trimmed rotor rotation speeds at each coupling cycle (from 0^{th} to 30^{th}) obtained by CAMRADII. In the initial transient cycles, the back-rotors' speed is much higher than the front-rotors' speed. However, as the coupling cycles reach the convergence state, the rotation speeds of all rotors are almost the same. For hover, the trim variables are the front-rotors rotation speed, the back-rotors rotation speed, and the airframe pitch angle. Table 2 lists these trim variables for the coupled solutions given by CAMRADII after the final coupling cycle, on the baseline and finer grids. For both grids, the airframe pitch angles are close to zero since the airframe forces and moments computed in CFD are not currently accounted for in CAMRADII, while the combined rotor forces and moments are well balanced. The trimmed rotor rotation speeds obtained on the finer-grid simulations are consistent with those obtained on the baseline grid, and the difference in the rotation speeds obtained on the two grids is less than 1%.

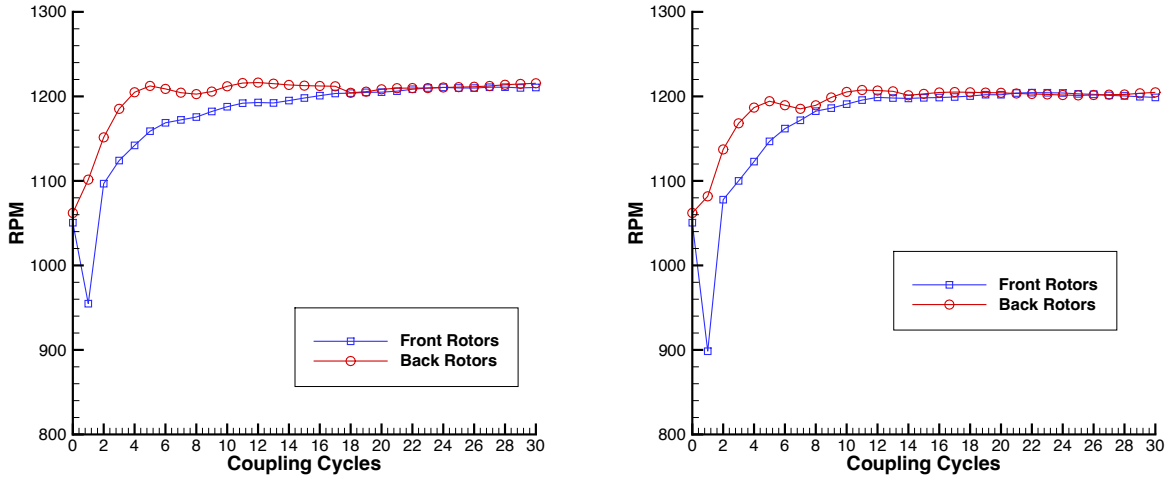

a. Baseline grid b. Finer grid

Figure 7. Convergence of rotor RPM trim in coupled simulations.

Table 2. Hover: Trim variables over the final coupling cycle.

Trim Variables	Baseline Grid	Finer Grid
Airframe Pitch Angle (degrees)	-0.05	-0.07
Front-rotors Speed (rpm)	1210.54	1198.79
Back-rotors Speed (rpm)	1215.51	1204.79

B. Rotor Performances

Figure 8 shows convergence of the FUN3D computed rotor thrust and torque versus rotor revolution for the outboard rotors (No. 1, 2, 7 and 8). Small variations of the thrust for the front-outboard rotors (No. 1 and 7) are still observed toward the end of baseline grid simulations, but the variations are less than 1%; the thrust and torque values in the finer grid simulations show relatively better convergence. Moreover, the thrust and torque acquired from axisymmetric pairs of rotors, i.e., rotors 1 and 7, as well as rotors 2 and 8, exhibit close matches, indicating that symmetric flowfield properties are maintained. Figure 9 shows convergence of the rotor thrust and torque versus rotor revolution for the inboard rotors (No. 3, 4, 5 and 6). These four rotors are canted at 8 degrees, such that the rotor wake flows toward the fuselage. With strong rotor wake and fuselage interactions, the thrust and torque values of these inboard rotors have not fully converged, but the differences between two adjacent coupling cycles are also less than 1%. More coupling cycles can be conducted to achieve a better convergence state. Similar to the outboard rotors, the inboard rotors also show maintenance of proper symmetric flowfield.

Table 3 lists the FUN3D predicted lifting rotor performances, in terms of thrust, torque and figure of merit (FM) over the final coupling cycle. Figure of merit is defined as $FM = \frac{C_T^{3/2}}{2\sqrt{C_P}}$, where C_T is the thrust coefficient and C_P is the power coefficient. Rotor thrust and torque are higher on the baseline grid, especially for the inboard rotors, where the wake interactions between rotors and fuselage are shown to be stronger with better resolution obtained on the finer grid. For the finer grid, the refined region extends well below the fuselage, resolving more wake interactions under the fuselage and rotors. This may be one of reasons the thrust and the torque of inboard rotors are lower on the finer grid. The total thrust of all rotors on the finer grid is closer to the aircraft weight of 5903 (lb). Compared to the baseline grid, the figures of

merit for the outboard rotors are higher, but lower for the inboard rotors on the finer grid, because stronger wake interactions with fuselage and consequently energy lost are better captured on the finer grid. Overall, the FM of all rotors are similar on the baseline and finer grids. The maximum difference is less than 1.4% at rotor 7.

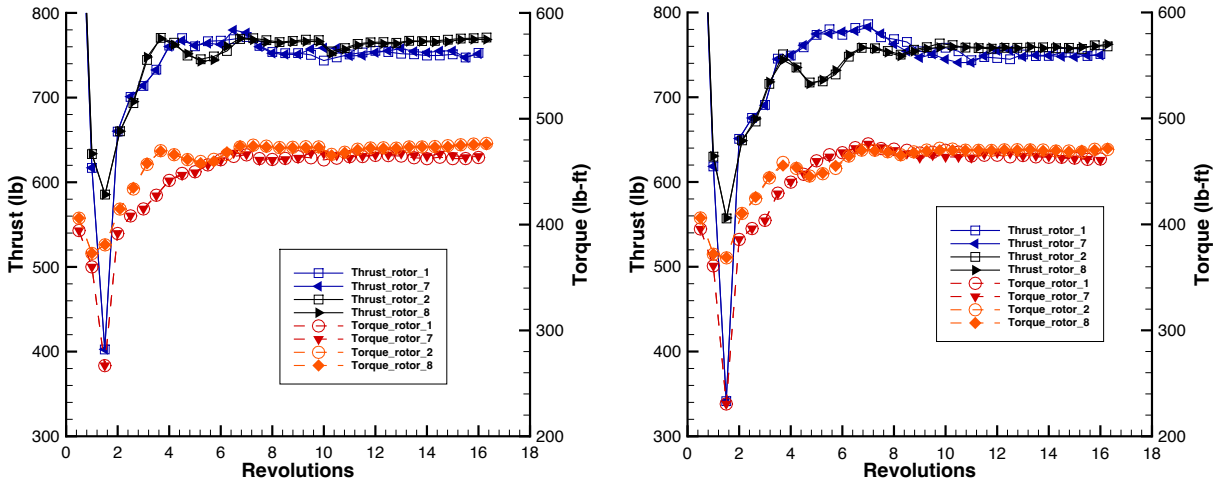

a. Baseline grid b. Finer grid

Figure 8. FUN3D thrust and torque predictions for outboard rotors.

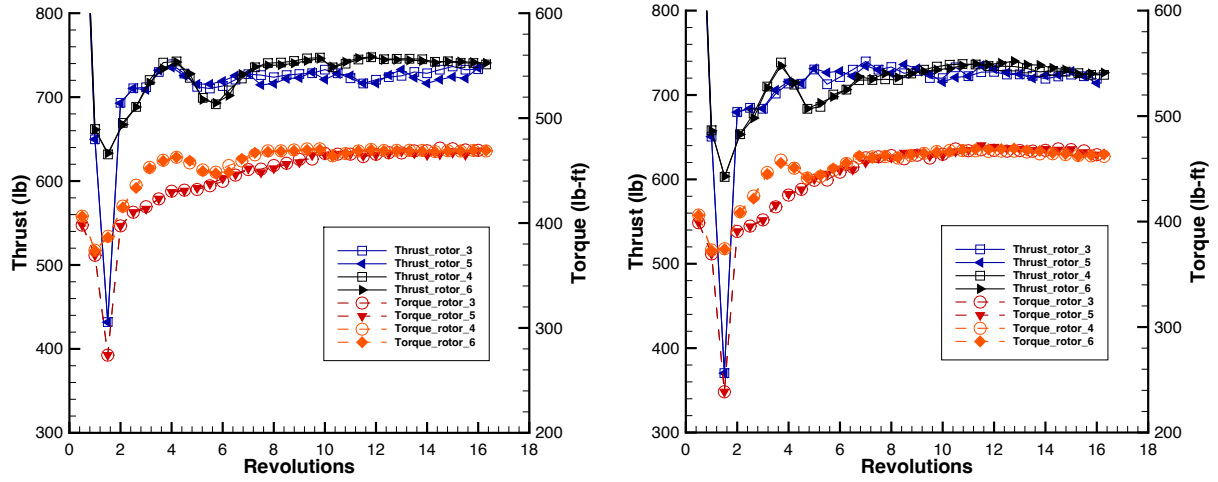

a. Baseline grid b. Finer grid

Figure 9. FUN3D thrust and torque predictions for inboard rotors.

Table 3. Hover: FUN3D predictions of lifting rotor performances.

	Baseline Grid			Finer Grid		
Rotor	Thrust (lb)	Torque (lb-ft)	FM	Thrust(lb)	Torque(lb-ft)	FM
1	752.80	463.39	0.6418	750.99	461.68	0.6481
2	770.93	476.69	0.6439	759.98	470.68	0.6440
3	733.25	469.27	0.6093	719.19	463.36	0.6052
4	738.95	468.68	0.6146	723.89	461.82	0.6101
5	734.80	468.95	0.6016	714.11	463.37	0.5988
6	740.78	469.19	0.6162	726.42	463.74	0.6108
7	751.65	464.56	0.6387	749.64	460.76	0.6476
8	768.62	475.85	0.6421	762.49	471.56	0.6459
Total	5991.78	3756.58		5906.71	3716.97	

Figures 10 and 11 show distributions of the sectional normal-force coefficient (M^2C_n) for the lifting rotors on the baseline and finer grids, viewing from the top of the aircraft, where the M is the Mach number and C_n is the normal force coefficient. For a single hovering rotor in a quasi-steady state, the normal forces are expected to be uniformly distributed over the azimuthal angles at any given radial location. For this lift+cruise concept aircraft, only forces in a small portion of the midspan regions are close to a uniform distribution. Wake interactions among lifting rotors and between the rotors and airframe strongly affect the forces in the rotor tip region. The forces at the rotor root region are affected by the supporting booms; the effects appear to be especially strong for the four front rotors (No. 1, 3, 5 and 7) as the wings and booms are located on the top of the front-rotor disks. On the finer grid, more details of the wake/fuselage interactions are observed and reflected in the forces for inboard rotors (No. 3, 4, 5 and 6). For this aircraft, a significantly unsteady flowfield is observed, with more details provided in the next section.

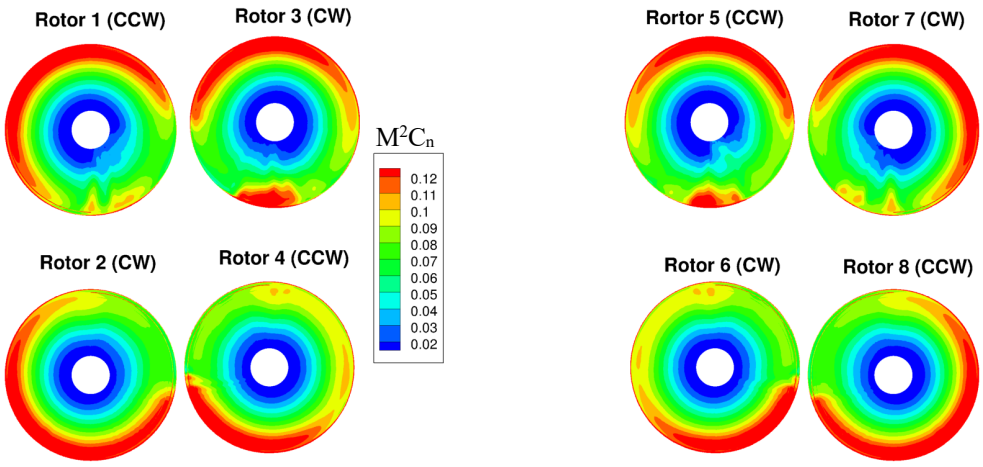

a. Left side of fuselage

b. Right side of fuselage

Figure 10. Hover: distributions of sectional normal force for rotors on the baseline grid (top view).

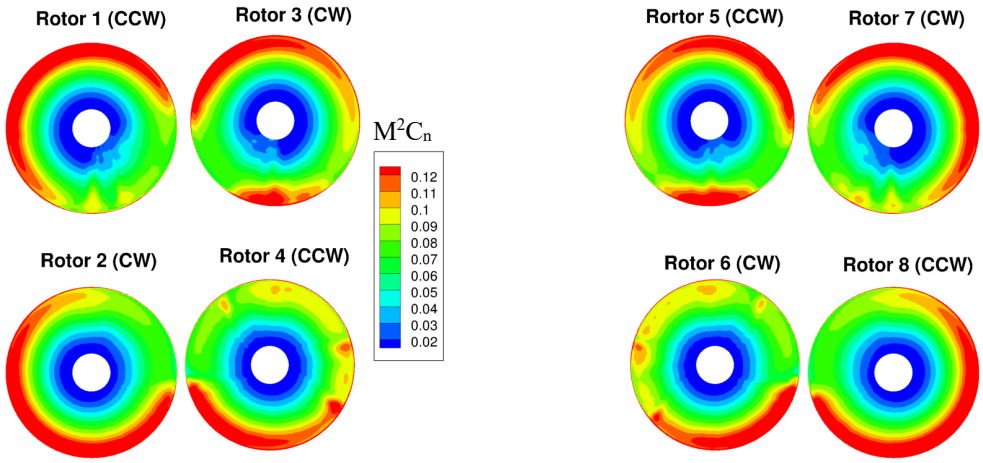

a. Left side of fuselage b. Right side of fuselage

Figure 11. Hover: distributions of sectional normal force for rotors on the finer grid (top view).

C. Airframe-Wingbody Forces

The forces on the rotor disk planes previously presented [34] and in section IV.B indicate rotor-to-rotor and rotor-to-airframe interactions for this multi-rotor aircraft in hover. In the current study, the workflow has been updated to compute and report the history of forces and moments in FUN3D on the prescribed airframe components. To study details of the unsteady aerodynamics, the lift+cruise aircraft airframe is divided into three groups: 1) fuselage with landing gear and vertical tail, 2) main wings, and 3) horizonal tail wings. The lift, drag and pitching moment coefficients for individual components are computed by FUN3D. Table 4 lists the reference values in CAMRADII, which are applied to convert nondimensional forces and moments to dimensional quantities. The center specified in FUN3D to compute the pitching moments is the same as the center of gravity of the entire aircraft, which is located at (12.0, 0.0, 0.0) listed in Table 1.

Table 4. Reference values.

	Values
Reference density	0.001911 slug/ft^3
Speed of sound	1135.84 *ft/sec*
Reference Mach number	0.4842
Reference length (rotor blade radius)	5.0 *ft*
Reference area (rotor disk area)	78.54 ft^2

Figures 12-17 show histories of the forces and moments on the airframe during the coupling cycles. The forces and moments on each airframe group are plotted and compared between the baseline and finer grids. Figure 12 shows the lift variations against revolutions, where lift is designated as the force along the positive z-axis direction for simplicity; Figure 13 shows histories of the lift during the final revolution. A strong downwash flow produced by the rotating rotors is observed, which causes large negative lift on both wings and fuselage. There is a large lift variation on the wings due to the rotor wake interactions. The dominant frequency is 2/rev, which is expected with two-bladed rotors. The amplitude of the lift on the wings varies from -1000 to -200 *lb* during one revolution, indicating the unsteadiness and strength of the rotor wake interactions. The lift variation on the fuselage is not as large as on the wings, but still significant for a non-

lifting surface. The lift on the horizontal tails is relatively small, given the nearly-zero aircraft pitch angle, implying little streamwise flow (x-direction) produced by the rotor wakes. Compared to the baseline grid, the lift on the fuselage and wings computed on the finer grid shows similar oscillation frequency and amplitude, but finer-grid results illustrate more wake interactions and more unsteady flow patterns during each revolution (Fig. 13). Although the influence of rotor wakes is relatively small on the tail wings, the lift calculated from the baseline grid is two times larger than the lift from the finer grid. As mentioned in section III.B, the refined grid region around the propeller blades applied on the baseline grid has been removed in the finer grid system. The purpose of this removal is to quickly dissipate the errors and disturbances generated by the overset grid interpolations around the static propeller blades and the background grid. This grid treatment is considered valid based on the assumption of minimal flow in that region during hover. A posteriori analysis indicates that additional grid refinement around the horizonal tails may be desired to more accurately capture the flowfield around both the tails and the propeller.

Figures 14 and 15 show the drag variation on the airframe during coupling cycles, where drag is designated as the horizontal force along the positive x-axis direction. The frequency of the drag variation remains consistent at 2/rev, but its amplitude is significantly smaller compared to the lift. There is some drag cancellation, with the fuselage contributing overall positive drag and wings generating negative drag. The drag on the tail wings is nearly zero. Figures 16 and 17 depict the variation in pitching moments on the airframe groups. As expected, the pitching moment on the wings has a large variation within one rotor revolution, while the pitching moment on the fuselage is comparatively small. The negative pitching moment produced by the vertical force on the tail wings are also noticeable; this is due to the substantial moment length for the tail wings. The tail-wing aerodynamics is of particular importance for the forward flight simulations, as it contributes to the stability of the aircraft and affects the overall vehicle performance.

Table 5 lists the averaged values of the forces and moments for the final revolution. The total averaged values of lift, drag and pitch moments on the airframe are reasonably close to each other between the baseline and finer grid results. The total negative lift from the airframe is close to 10% of the vehicle weight, and the negative pitch moment is non-negligible. Currently, CAMRADII assumes the airframe forces and moments are zero in the trim cycles for hover. The FUN3D/CAMRADII coupling workflow needs to be improved so that the total averaged values of the airframe forces and moments predicted by FUN3D can be provided for the CAMRADII trim.

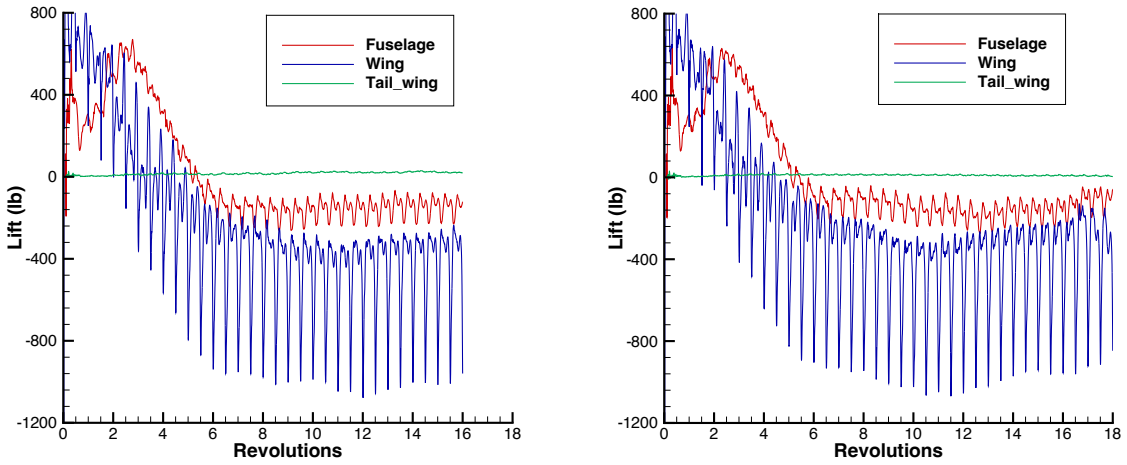

a. Baseline grid

b. Finer grid

Figure 12. FUN3D lift force predictions for airframe.

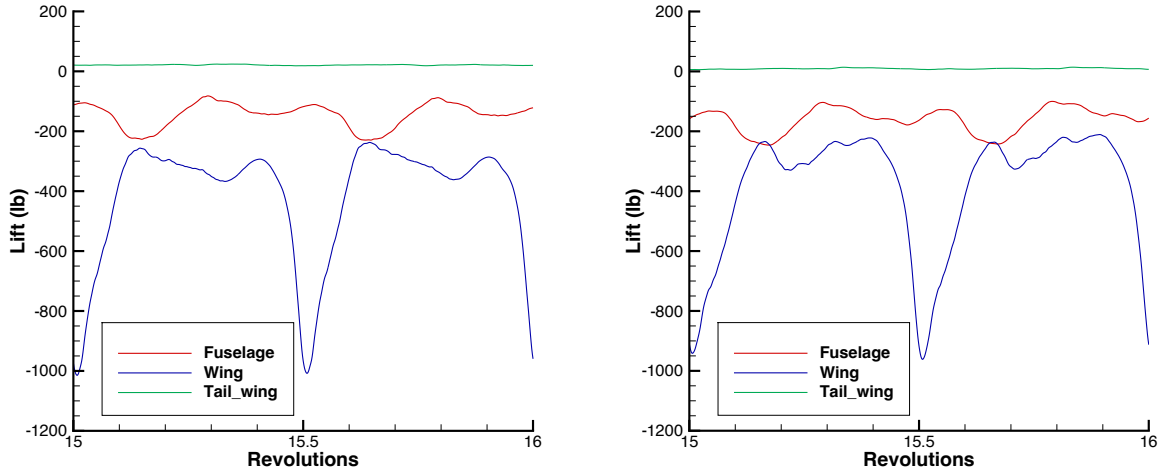

a. Baseline grid b. Finer grid

Figure 13. FUN3D lift force predictions over the final revolution.

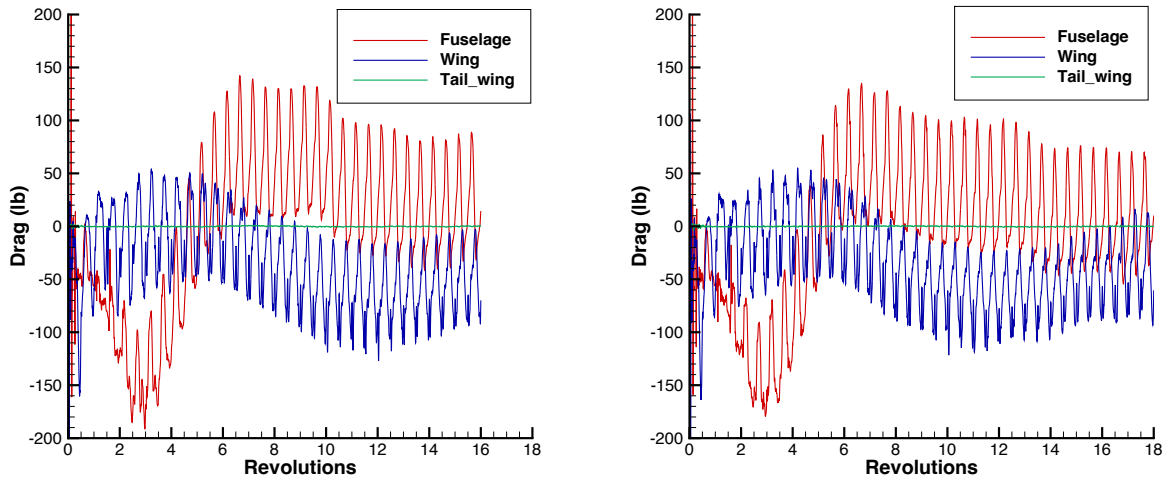

a. Baseline grid b. Finer grid

Figure 14. FUN3D drag force predictions for airframe.

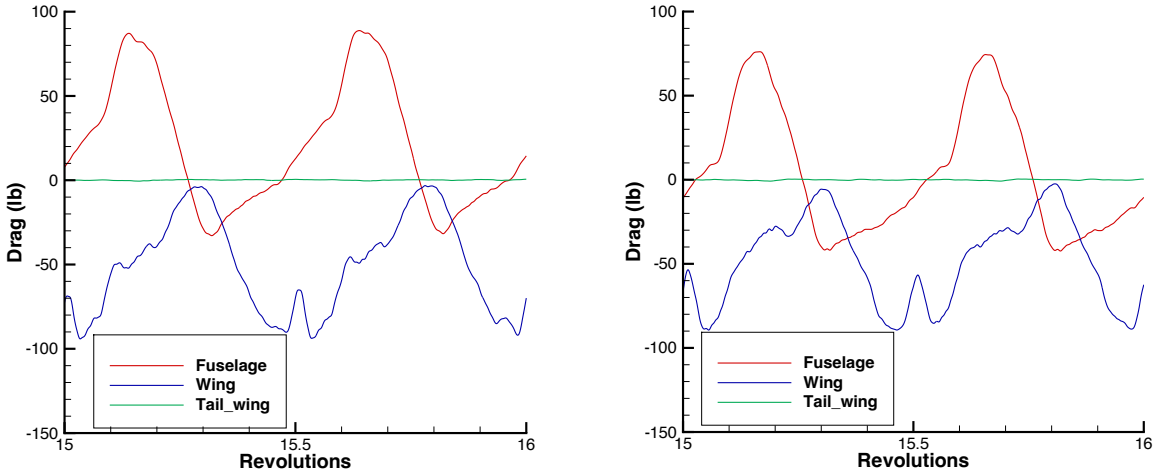

a. Baseline grid b. Finer grid

Figure 15. FUN3D drag force predictions over the final revolution.

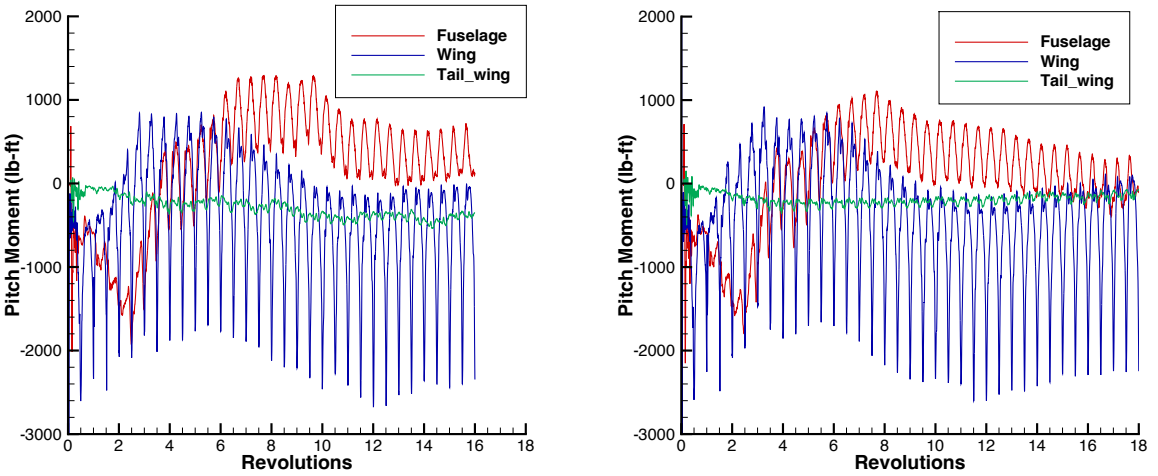

a. Baseline grid b. Finer grid

Figure 16. FUN3D pitching moment predictions for airframe.

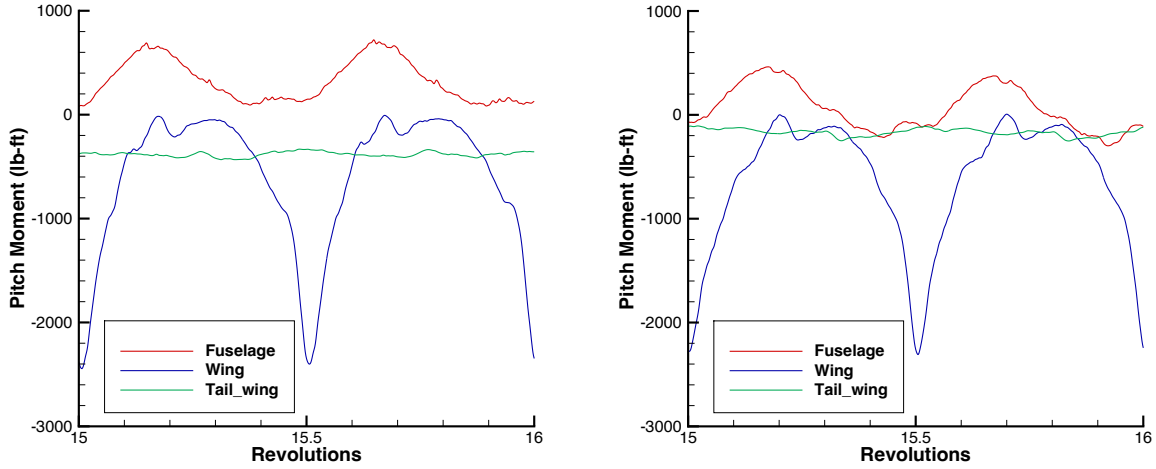

a. Baseline grid b. Finer grid

Figure 17. FUN3D pitching moment predictions over the final revolution.

Table 5. Hover: FUN3D average forces and moments for airframe.

	Baseline Grid			Finer Grid		
Airframe component	Lift (lb)	Drag (lb)	Pitching moment (lb-ft)	Lift (lb)	Drag (lb)	Pitching moment (lb-ft)
Fuselage	-144.77	20.79	324.38	-161.70	4.18	62.58
Wings	-417.49	-51.24	-608.69	-388.97	-48.47	-638.18
Tail-wings	21.17	0.13	-382.05	9.35	-0.08	-168.33
Total	-541.09	-30.32	-666.36	-541.32	-44.37	-743.93

D. Wake Structures

Figures 18, 19 and 20 show isosurfaces of Q-criterion (at value of 0.002, which is four times larger than the value used in the previous study [34]) colored by the vorticity magnitude for the baseline and finer grids at the end of 30th coupling cycle, viewed from different directions. In the baseline-grid case, the tip vortices generated by the lifting rotors are successfully captured, including details of secondary vortices and wake interactions. The pronounced wake/fuselage interactions from the inboard rotors (No. 3, 4, 5, and 6) canted at 8 degrees are also well resolved. However, the inboard rotor wake interactions beneath the fuselage are only accurately captured with the finer grid containing a substantially larger region of clustered points.

On the baseline grid, there is a vortex structure observed near the propeller region, consistent with the findings in our previous study. A possible source of the structure is the flow interactions between the vertical tail and the stationary propeller blades. Another possibility is overset grid interpolation errors, which may not dissipate quickly enough due to the refined grid region near the propeller and near-quiescent flow in the region to carry away the errors downstream. To increase dissipation in that area, the clustering around the propeller has been eliminated in the finer grid, resulting in a significant reduction in the flow disturbances (shown in Figs. 19 and 20). However, as shown in Table 5, the pitching moments from the tail wings are sensitive to the variations of the vertical force and some grid refinement around the vertical and horizonal tails may still be necessary for improved predictions of airframe aerodynamics.

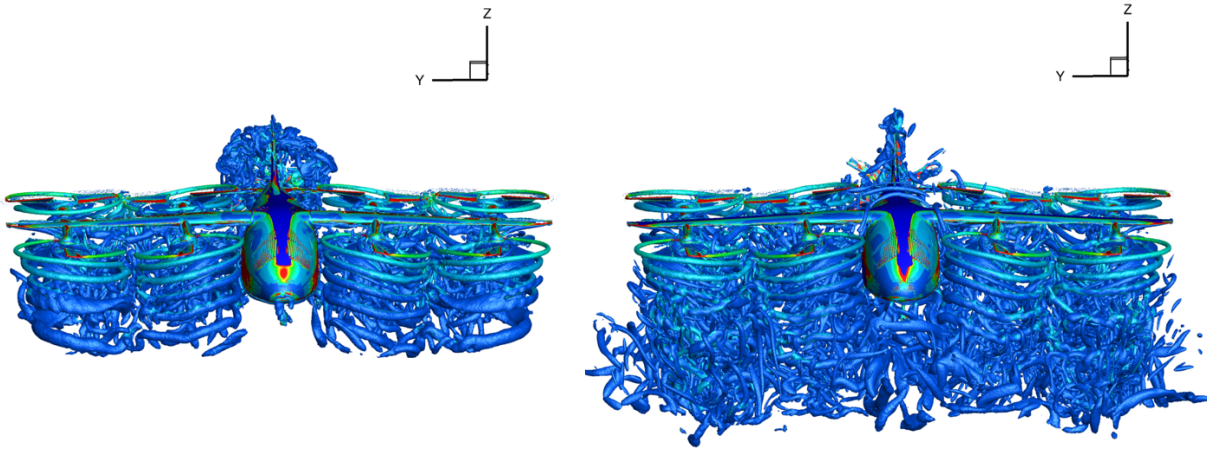

a. Baseline grid b. Finer grid

Figure 18. Front view: isosurfaces of Q-criterion colored by vorticity magnitude around the lift+cruise concept aircraft in hover.

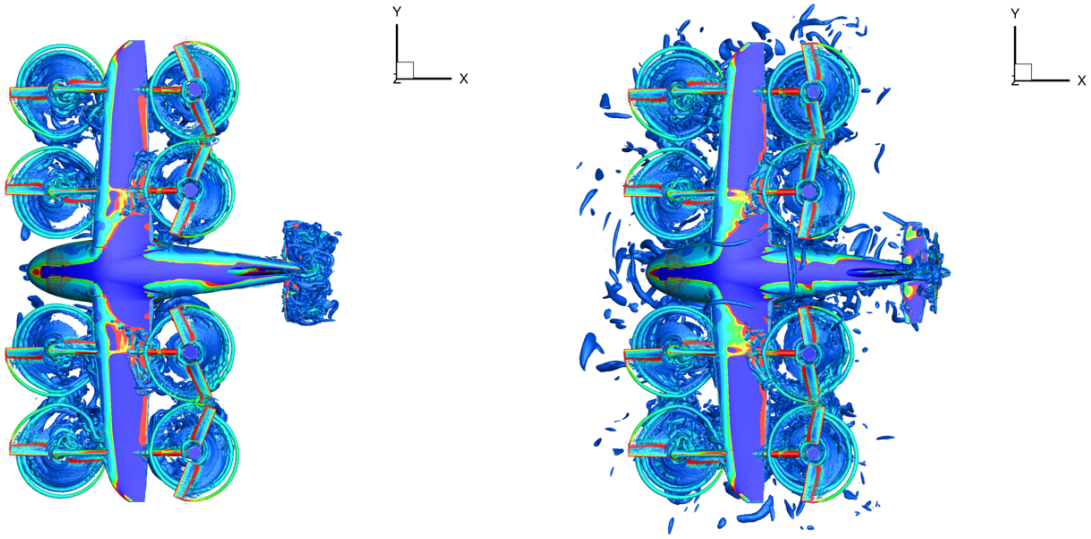

a. Baseline grid b. Finer grid

Figure 19. Top view: isosurfaces of Q-criterion colored by vorticity magnitude around the lift+cruise concept aircraft in hover.

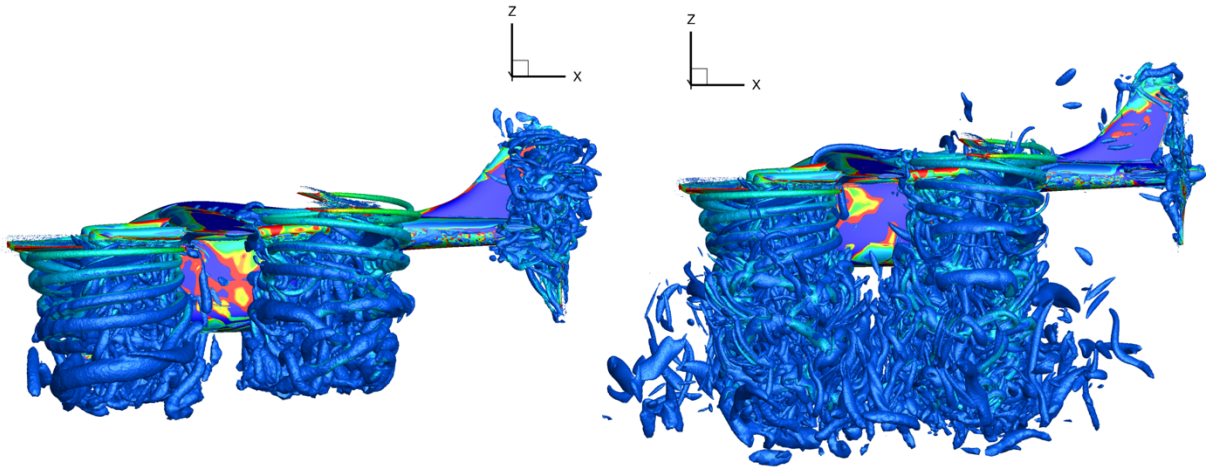

a. Baseline grid b. Finer grid

Figure 20. Side view: isosurfaces of Q-criterion colored by vorticity magnitude around the lift+cruise concept aircraft in hover.

E. Computational Cost

All simulations in the current work have been performed at the NASA Advanced Supercomputing (NAS) facility at NASA Ames Research Center. The computations for the baseline grid were conducted using 3,000 Pleiades Haswell processing cores. For the finer grid, the computations used 7,200 Electra Skylake processing cores. The nominal computational cost was 18-20 wall-clock hours for one rotor revolution, each of which included two loose-coupling cycles between FUN3D and CAMRADII.

V. Concluding Remarks

High-fidelity simulations have been performed for the NASA lift+cruise VTOL UAM concept aircraft in hover using variable-rotor rotation-speed trim. The multidisciplinary simulations are based on loose coupling of the FUN3D CFD solver and the CAMRADII comprehensive analysis model. The SA-neg-R turbulence model described at the NASA turbulence modeling resource website[**] is used. The CFD solutions have been computed on composite unstructured-grid systems using a scalable grid assembler, Yoga. Two grid systems, a baseline grid with approximatively 200 million grid points and a finer grid with 394 million grid points, have been considered. This work improves the FUN3D/CAMRADII coupling workflow for computing and reporting the forces and moments on airframe components.

The solutions from the rotor disk planes and the airframe components reveal a strong unsteady flowfield surrounding the lift+cruise aircraft during hover. The flow interactions between rotor wakes and the airframe lead to significant fluctuations in the forces and moments on the fuselage and wings. The averaged values of these aerodynamic quantities deviate substantially from zero, highlighting the need to incorporate them in the trim procedure. For the coupled analyses on both grids, the trim rotation speeds for front and back rotors evaluated by CAMRADII are closely aligned in the end of the coupling procedure. Similarly, the forces and moments on the airframe obtained on the two grids exhibit consistency in terms of the averaged values and the dominant frequency. The rotor thrust and torque computed on the baseline grid are generally higher than those on the finer grid, particularly for the inboard rotors. The solution obtained on

[**] https://turbmodels.larc.nasa.gov/spalart.html; Accessed October 2023

the finer grid, characterized by a refined grid zone extending well below the fuselage, captures more flow features of the inboard rotor wakes and their interactions with the fuselage as well as downwash effects.

This work demonstrates the capabilities of a high-fidelity, multidisciplinary analysis tool for simulations of complex multi-rotor lift+cruise aircraft in hover, with reasonable predictions of rotor performance and airframe aerodynamics. For the future work, the coupling workflow will be improved by computing the averaged forces and moments on the airframe and providing them to CAMRADII for trimming considerations at each coupling cycle. Furthermore, hybrid RANS(SA-neg-R)/large-eddy-simulation (LES) will be employed to analyze rotor-hover performance on finer grids (after incorporating enhanced mesh resolution in the tail regions). That level of resolution is likely sufficient for hybrid RANS/LES. Further verification and validation can also be performed with comparisons with experimental or other computational data when they become available.

Acknowledgments

The NASA Revolutionary Vertical Lift Technology (RVLT) project funded the work reported here. The authors would like to thank Dr. Douglas Boyd and Dr. Brian Allan from the NASA Langley Research Center for their help on the CAMRADII models and the lift+cruise aircraft surface geometry specifications.

References

[1] Hariharan N., Egolf T.A., Sankar, L.N., "Simulation of Rotor in Hover: Current State and Challenges," AIAA 2014-0041, 2014. https://doi.org/10.2514/6.2014-0041

[2] AIAA Rotorcraft Hover Prediction Workshop. https://www.aiaa-hpw.org

[3] Balch, D. T. and Lombardi, J., "Experimental Study of Main Rotor Tip Geometry and Tail Rotor Interactions," NASA Contractor Report 177336, February 1985.

[4] Wong, O. D., Noonan, K. W., Watkins, A. N., Jenkins, L. N., Yao, C-S, "Non-Intrusive Measurements of a Four-Bladed Rotor in Hover – A First Look," American Helicopter Society Aeromechanics Specialists' Conference, San Francisco, CA, January 20-22, 2010.

[5] Overmeyer, A.D., Copp P.A., and Schaeffler, N.W., "Hover Validation and Acoustic Baseline Blade Set Definition," NASA/TM–2020–5002153, May 2020.

[6] Wissink, A.M., Sitaraman, J., Jayaraman B., Roget, B., Lakshminarayan, V.K., Potsdam M., Jain R., Bauer, A., and Strawn, R., "Recent Advancements in the Helios Rotorcraft Simulation Code," AIAA 2016-0563, 2016. https://doi.org/10.2514/6.2016-0563.

[7] Jain, R., "Sensitivity Study of High-Fidelity Hover Predictions on the Sikorsky S-76 Rotor", *Journal of Aircraft*, Vol. 55, No. 1 (2018), pp. 78-88. https://doi.org/10.2514/1.C034076.

[8] Overmeyer, A. and Martin, P.B., "The Effect of Boundary Layer Transition on Rotor Hover Performance at Model Scale," AIAA 2017–1872, 2017. https://doi.org/10.2514/6.2017-1872.

[9] Jain, R., "CFD Performance and Turbulence Transition Predictions on an Installed Model-scale Rotor in Hover," AIAA 017-1871, 2017. https://doi.org/10.2514/6.2017-1871.

[10] Lee, B., Jung, Y.S., Jude, D., and Baeder, J.D., "Turbulent Transition Prediction of PSP Hovering Rotor Using γ-$Re_{\theta t}$-SA with Crossflow Transition Model," AIAA 2019-0286, 2019. https://doi.org/10.2514/6.2019-0286.

[11] Jared, C., and Coder, J.G., "Effects of Crossflow Transition on the S-76 and PSP Rotors in Hover," AIAA 2020-0773, 2020. https://doi.org/10.2514/6.2020-0773.

[12] Park, S., Kwon, O., "Numerical Study of Isolated and Full Configuration PSP Rotor Using a Mixed Mesh Flow Solver," AIAA-2020-0529, 2020. https://doi.org/10.2514/6.2020-0529.

[13] Sheng, C., Zhao, Q., Baugher, S., "Numerical Investigation of Rotor Aerodynamics Using High-Order Unstructured Grid Schemes," AIAA 2020-0528, 2020. https://doi.org/10.2514/6.2020-0528.

[14] Narducci, R. P., Jain, R., Abras, J., and Hariharan, N., "HVAB Rotor Hover Computational Prediction: A Comparative Study Using OVERFLOW and HPCMP CREATE™-AV Helios," AIAA 2021-0617, 2021. https://doi.org/10.2514/6.2021-0617.

[15] Zhao, Q., and Sheng, C., "Predictions of HVAB Rotor in Hover Using Hybrid RANS/LES Methods," AIAA 2021-0618, 2021. https://doi.org/10.2514/6.2021-0618.
[16] Park, S. H., Han, J., and Kwon, O. J., "Numerical Study of HVAB Rotor Using a Mixed Mesh Flow Solver," AIAA 2021-0619, 2021. https://doi.org/10.2514/6.2021-0619.
[17] Quackenbush, T.R., Whitehouse. G.R., Silabaugh, B.S., Yu, M.K., "Further Assessment of Analysis Methods for Rotor/Airframe Interaction in Hover," AIAA 2018-1783, 2018. https://doi.org/10.2514/6.2018-1783.
[18] Quackenbush, T.R., Whitehouse, G.R., "Analysis of Rotor/Airframe Interaction in Hover and Near-Hover Flight Conditions," AIAA 2019-0596, 2019. https://doi.org/10.2514/6.2019-0596.
[19] Pérez, A., Lopez, O., Poroseva, S., Escobar, J.A., "Free-Vortex Wake and CFD Simulation of a Small Rotor for a Quadcopter at Hover," AIAA 2019-0597, 2019. https://doi.org/10.2514/6.2019-0597.
[20] Patterson, M. D., Antcliff, K. R., and Kohlman, L. W., "A Proposed Approach to Studying Urban Air Mobility Missions Including an Initial Exploration of Mission Requirements." American Helicopter Society 74th Annual Forum, Phoenix, AZ, May 2018.
[21] Silva, C., Johnson, W., Antcliff, K. R., and Patterson, M. D., "VTOL Urban Air Mobility Concept Vehicles for Technology Development." AIAA 2018-3847, 2018. https://doi.org/10.2514/6.2018-3847
[22] Antcliff, K., Whiteside, S., Silva, C., and Kohlman, L., "Baseline Assumptions and Future Research Areas for Urban Air Mobility Vehicles," AIAA 2019-0528, 2019. https://doi.org/10.2514/6.2019-0528
[23] Whiteside, S. K. S., Pollard, B. P., Antcliff, K. R., Zawodny, N. S., Fei, X., Silva, C. and Medina, G.L., "Design of a Tiltwing Concept Vehicle for Urban Air Mobility." NASA TM20210017971, June 2021.
[24] Johnson, W. and Silva, C., "Observations from Exploration of VTOL Urban Air Mobility Designs," The Asian/Australian Rotorcraft Forum, 2018.
[25] Diaz, P. V., Ahmad, J., and Yoon, S., "The Side-by-Side Urban Air Taxi Concept," AIAA 2019-2828, 2019. https://doi.org/10.2514/6.2019-2828
[26] Diaz, P. V., Perez, D. P., and Yoon, S., "Computational Analysis of a Quiet Single-Main Rotor Helicopter for Air Taxi Operations", Vertical Flight Society 78th Annual Forum, Dallas, Texas, May 2022.
[27] Diaz, P. V., and Yoon, S., "Computational Study of NASA's Quadrotor Urban Air Taxi Concept," AIAA 2020-0302, 2020. https://doi.org/10.2514/6.2020-0302
[28] Perez, D. G., Diaz, P. V., and Yoon, S., "High-Fidelity Simulations of a Tiltwing Vehicle for Urban Air Mobility", AIAA 2023-2282, 2023. https://doi.org/10.2514/6.2023-2282
[29] Nichols, R. H., Tramel, R. W., and Buning, P. G., "Solver and Turbulence Model Upgrades to OVERFLOW 2 for Unsteady and High-Speed Applications," AIAA 2006–2824, 2006. https://doi.org/10.2514/6.2006-2824
[30] Johnson, W., "Rotorcraft Aerodynamic Models for a Comprehensive Analysis," American Helicopter Society 54th Annual Forum, Washington D.C., May 1998.
[31] Caprace, D., Ventura Diaz, P., and Yoon, S., "Simulation of a Single Rotor and a Quadrotor Hovering in Full and Partial Ground Effect," AIAA 2023-4281, 2023. https://doi.org/10.2514/6.2023-4281
[32] Druyor, C. T., and Wang, L., "High-Fidelity Analysis of Six-Passenger Quadrotor Air Taxi Concept." Vertical Flight Society 78th Annual Forum, Fort Worth, TX, May 2022.
[33] Anderson, W. K., Biedron, R. T., Carlson, J.-R., Derlaga, J. M., Druyor C. T., Jr., Gnoffo, P. A., Hammond, D. P., Jacobson, K. E., Jones, W. T., Kleb, B., Lee-Rausch, E. M., Nastac, G. C., Nielsen, E. J., Park, M. A., Rumsey, C. L., Thomas, J. L., Thompson, K. B., Walden, A. C., Wang L., , Wood, S. L., Wood, W. A., Diskin, B., Liu, Y., Zhang, X., "FUN3D Manual: 14.0," NASA TM 20220017743, 2022. https://fun3d.larc.nasa.gov/papers/FUN3D_INTG_Manual-14.0.pdf
[34] Liu, Y., Druyor, C. T., and Wang, L., "High-Fidelity Analysis of Lift+Cruise VTOL Urban Air Mobility Concept Aircraft," AIAA 2023-3671, 2023. https://doi.org/10.2514/6.2023-3671

[35] Allmaras, S. R., Johnson, F. T., and Spalart, P. R., "Modifications and Clarifications for the Implementation of the Spalart-Allmaras Turbulence Model," ICCFD7-1902, 7th International Conference on Computational Fluid Dynamics, Big Island, Hawaii, 9-13 July 2012. https://www.iccfd.org/iccfd7/assets/pdf/papers/ICCFD7-1902_paper.pdf
[36] Dacles-Mariani, J., Zilliac, G. G., Chow, J. S., and Bradshaw, P., "Numerical/Experimental Study of a Wingtip Vortex in the Near Field," *AIAA Journal*, Vol. 33(9), 1995, pp. 1561-1568. https://doi.org/10.2514/3.12826
[37] Dacles-Mariani, J., Kwak, D., and Zilliac, G. G., "On Numerical Errors and Turbulence Modeling in Tip Vortex Flow Prediction," *Int. J. for Numerical Methods in Fluids*, Vol. 30(1), 1999, pp. 65-82. https://doi.org/10.1002/(SICI)1097-0363(19990515)30:1<65::AID-FLD839>3.0.CO;2-Y
[38] Abdol-Hamid, K. S., Carlson, J.-R., Rumsey, C. L., Lee-Rausch, E. M., and Park, M. A., "DPW-6 Results Using FUN3D With Focus on k-kL-MEAH2015 Turbulence Model," AIAA 2017-0962, 2017. https://doi.org/10.2514/6.2017-0962
[39] Chwalowski, P. and Heeg, J., "FUN3D Analyses in Support of the Second Aeroelastic Prediction Workshop," AIAA 2016-3122, 2016. https://doi.org/10.2514/6.2016-3122
[40] Silva, W. A., Sanetrik, M. D., and Chwalowski, P., "Using FUN3D for Aeroelatic, Sonic Boom, and AeroPropulsoServoElastic (APSE) Analyses of a Supersonic Configuration," AIAA 2016-1319, 2016. https://doi.org/10.2514/6.2016-1319
[41] Jain, R., Biedron, R. T., Jones, W., and Lee-Rausch, E. M., "Modularization and Validation of NASA FUN3D as a HPCMP CREATE-AV Helios Near-body Solver," AIAA 2016-1298, 2016. https://doi.org/10.2514/6.2016-1298
[42] Nielsen, E. J., "Adjoint-Based Aerodynamic Design of Complex Aerospace Configurations," ASME 2016 Fluids Engineering Division Summer Meeting, FEDSM 2016–7573, July 2016.
[43] Roe, P. L., "Approximate Riemann Solvers, Parameter Vectors, and Difference Schemes," *Journal of Computational Physics*, Vol. 43, No. 2, 1981, pp. 357–372. https://doi.org/10.1016/0021-9991(81)90128-5
[44] Burg, C. O. E., "Higher Order Variable Extrapolation for Unstructured Finite Volume RANS Flow Solvers," AIAA Paper 2005–4999, 2005. https://doi.org/10.2514/6.2005-4999
[45] van Leer, B., "Towards the Ultimate Conservative Difference Scheme, V. A Second Order Sequel to Godunov's Method," *Journal of Computational Physics*, Vol. 32, No. 1, 1979, pp. 101–136. https://doi.org/10.1016/0021-9991(79)90145-1
[46] Haselbacher, A. C., "A Grid-Transparent Numerical Method for Compressible Viscous Flow on Mixed Unstructured Meshes," Ph.D. thesis, Loughborough University, 1999. https://hdl.handle.net/2134/7257
[47] Nishikawa, H., "Beyond Interface Gradient: A General Principle for Constructing Diffusion Schemes", AIAA 2010-5093, 2010. https://doi.org/10.2514/6.2010-5093
[48] Vatsa, V., Carpenter, M. H., and Lockard, D., "Re-evaluation of an Optimized Second Order Backward Difference (BDF2OPT) Scheme for Unsteady Flow Applications," AIAA 2010–0122, 2010. https://doi.org/10.2514/6.2010-122
[49] Druyor, C., "Enhancing Scalability for FUN3D Rotorcraft Simulations with Yoga: An Overset Grid Assembler," AIAA 2021-2746, 2021. https://doi.org/10.2514/6.2021-2746
[50] Johnson, W., and Silva, C., "NASA Concept Vehicles and the Engineering of Advanced Air Mobility Aircraft," *The Aeronautical Journal (2022)*, 126, pp. 59-91, https://doi.org/10.1017/aer.2021.92
[51] Biedron, R. T. and Lee-Rausch, E. M., "Rotor Airloads Prediction Using Unstructured Meshes and Loose CFD/CSD Coupling," AIAA 2008–7341, 2008. https://doi.org/10.2514/6.2008-7341